

## Buckling of Structures with Interacting Propagating Cracks

D.C. Tran and A. Limam  
Laboratory LGCIE  
INSA de Lyon, Villeurbanne, France

### Abstract

The development of energy absorbers by “tearing” or “splitting” circular tubes demonstrates that in certain cases an instability corresponding to the wrinkling of the free edges or the crack lips developed behind the crack tip. These undulations of buckling have a wave length which depends on the geometrical characteristics of the tube and the velocity at which the tear propagates. In order to understand the origins of this phenomenon associated to the buckling of “free edges”, several quasi-static experiments with various geometries of stainless steel tubes (diameter to thickness ratios) are conducted. Over-sized rigid dies are pushed inside the tubes along their axes to generate fractures in Mode I. As the crack propagates, wrinkles develop on the crack lips. Numerical modelling is also considered. It couples various nonlinearities, such as large displacements necessary to the buckling analysis, plasticity and fracture in order to reproduce the ductile tearing and surface contacts associated with specific boundary conditions. Simulations are conducted with the ABAQUS Standard code. To manage crack propagation, two fracture models such as the cohesive zone model (CZM) and the damage model (DM) are used.

**Keywords:** cohesive zone model, damage model, buckling, ductile fracture, contact, metal tube tearing.

### 1 Introduction

When one uses a tool to cut a sheet metal, or a tube according to his axis, sometime, buckling waves appear on the free edges. This wavy edge bears strong similarities with the geometry on the wreckage of some aircraft fuselage skins associated to destroyed aircraft [1]. In order to understand this behavior, we conducted a set of experiments, in which stainless steel tubes are cut according to a generatrice. An adequate instrumentation, including specific measurements (strain gages, digital

image correlation) allowed us accurately to put forward the phenomenology, in particular the kinematics at the scale of the crack (ahead of crack tip) and at the level of tube (wave lengths of buckling). Various geometries of tubes (Diameter/thickness) were tested. The numerical simulation take into account large displacement as buckling phenomenon is involved and material nonlinearities, material yielding associated to ductile tear propagation. The implicit method is considered. The crack propagation is managed by the cohesive zone model (CZM) or by the damage model (DM). The coupling of solid elements, shell continuum elements and these fracture models makes it possible to corroborate the experimental observations. The assumption of the mode I crack propagation is made. It's still a challenge to get the cohesive parameters (separation energy, cohesive strength), or the ductile damage parameters (fracture strain, displacement at failure) experimentally on thin sheets, thus these material properties managing the cracking are obtained by numerical retiming. These studies show that the displacement of cutting tool induced a circumferential extension of the tube that leads to a local necking in the radial direction bringing the rupture finally. During the failure, a "plastic wake" appears, relatively wide, close and parallel to crack lips. Constrained by other parts of the tube which remain elastic, sufficient axial residual compressive stresses produced in this plastic wake produce the undulations which represents a local buckling.

## **2 Experimentation**

### **2.1 Experimental program**

Splitting tests of stainless steel tubes 304L, were carried out under quasi-static conditions. The laboratory test bench is illustrated in Figure 1. This bench contains a system of boundary conditions allowing fixing the tube, a system of loading to tear the tube, a system of measurement (camera, gage and sensors) to determine the force, displacement of the cutting tool and the field deformation of the tube. Figure 2 shows a zoom on the assembly of cone, tube, joint and steel bar. Two geometries are studied with dimensions (outside diameter x wall thickness) of 50x1.5mm and 48.3x2mm. The cutting tool, an asymmetrical cone (Figure 3), considered to be rigid compared to the tube, is translated in the tube along its axis, in order to produce a propagation of the crack. In the test, one end of the tube is fixed; the cone is positioned at the other end so that its maximum diameter coincides with the initial crack position on the tube. This initial crack is a saw-cut 20mm long, 2mm wide and V-shaped at the tip. It is created by a saw at one end of the tube along a generator. And it is located contrary to the presented welding on the stainless tubes. The displacement of the cone is ensured by a cylindrical steel bar connected to a hydraulic servo-jack. The cone is pushed at a constant speed of 5mm/min for 250mm of stroke into the 300mm long tube. Two configurations of experimental condition are studied: with lubrication, without lubrication on the surface of the cone and the tube.

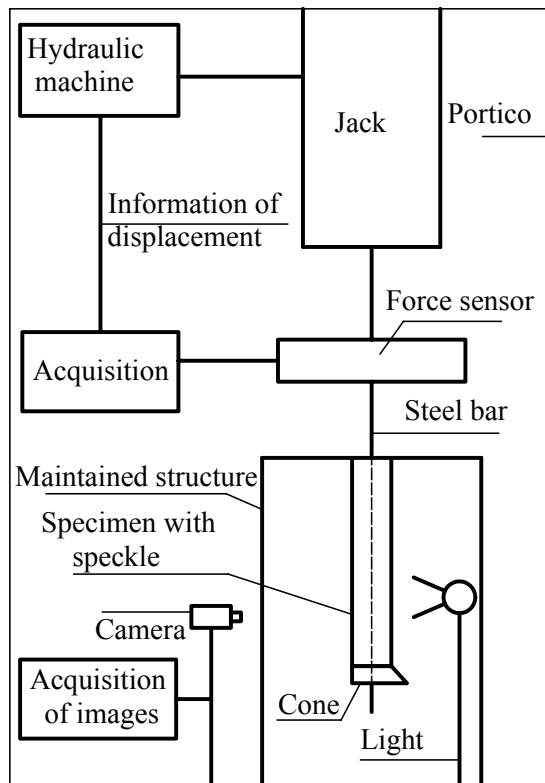


Figure 1: Laboratory test bench

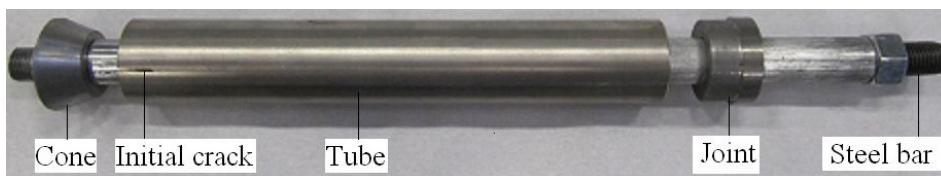


Figure 2: Assembly of Cone, Tube with initial crack, Joint, Steel bar

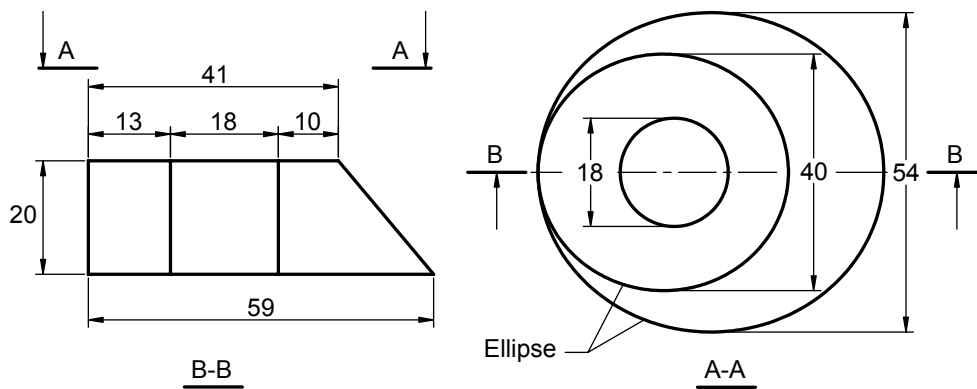


Figure 3: Dimensions of the cone (mm)

The material behavior is characterized via uniaxial tensile tests carried out at room temperature and realized on test-tubes cutout according to the axial direction of the tubes. The tests are controlled in displacement at a constant speed of 1,2mm/min and are instrumented using high elongation strain gages coupled with extensometer. The tests give: Young's modulus  $E=186\text{GPa}$ , Poisson's ratio  $\nu=0.3$ , proof strength  $R_{p0.2}=419\text{MPa}$ , tensile strength  $R_m=752\text{MPa}$ , ultimate strain  $A=43\%$ , Figure 4 shows a characteristic stress-strain curve.

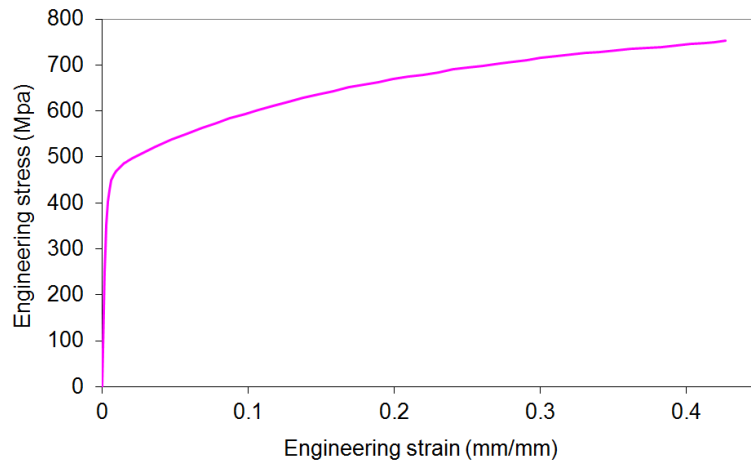


Figure 4: Engineering stress-strain curve for stainless steel 304L

## 2.2 Results

### 2.2.1 Deformation of the tube

Behind the crack tip, we note the appearance of undulations on the crack lips, the mode is sometimes symmetrical, and sometimes a different phase of the waves appears from the first undulation (Figure 5).

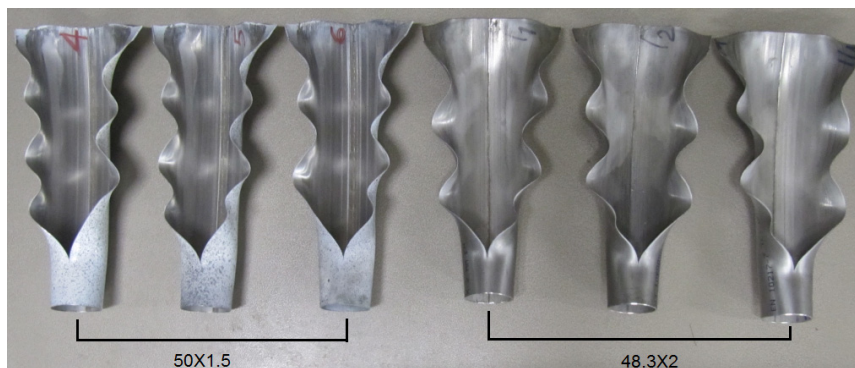


Figure 5: Deformed shapes of tube for different  $D/t$

To better apprehend the undulating behavior of the fractured edges, one took a measure, via high elongation strain gages allowing the measurement of the longitudinal deformation in a point located at 150mm from the fixed end of the tube and on a generator located at 30° from the crack line (Figure 16). The digital image correlation method is used to measure the displacement fields with assistance of a VIC3D system. A deflection in hollow is noted ahead of crack tip as well as a strong variation of the deformation in regions adjacent to the crack tip (Figure 6).

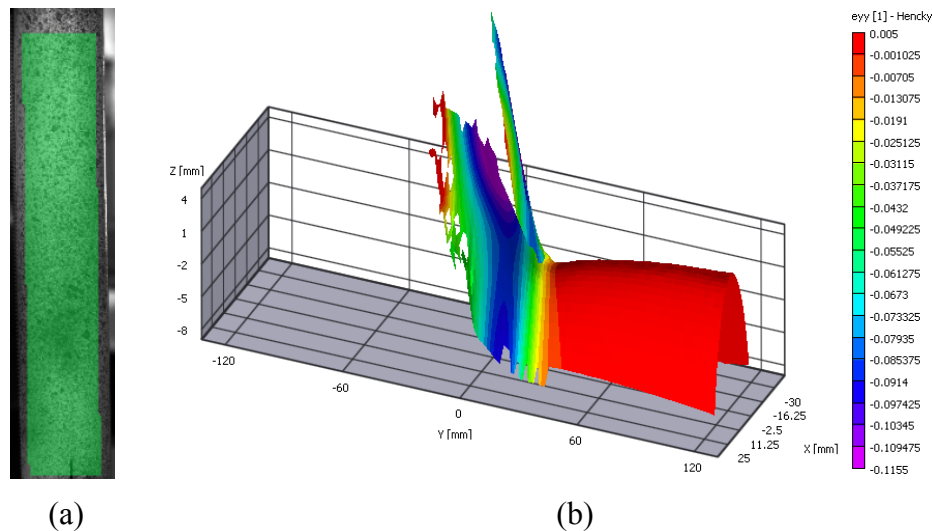


Figure 6: Axial deformation at the cone position  $y = 150\text{mm}$ , (a) zone studied, (b) axial deformation  $\epsilon_{yy}$

## 2.2.2 Load-displacement curves

Figure 7 visualizes the various load-displacement curves of the cone for different geometries of tube. The combination of the pressure and sliding at the contact surface is such that the lubricant tends to be removed from this surface so that the tube and cone seem dry after the test. We note that lubrication influences only the first translation of the cone where the state of contact is not stable yet.

The load-displacement curve behavior can be divided into three stages. Figure 8 shows a typical analysis of the tube 50x1.5 with lubrication. Two first steps can be qualified as unstable or transients phases. The third is more stable, it expresses a permanent contact between the tube and the cone. During the first stage, only the leading edge of the tube is in contact with the cone. The unloading is a consequence of both the large geometry changes and the changing angle of contact at the leading edge. A second unloading occurs during the stage 2 for which the leading edge is not anymore in contact with the cone. It is due to combination of the inflection, the change of the surface contact and the propagation of crack which decreases the rigidity of the structure.

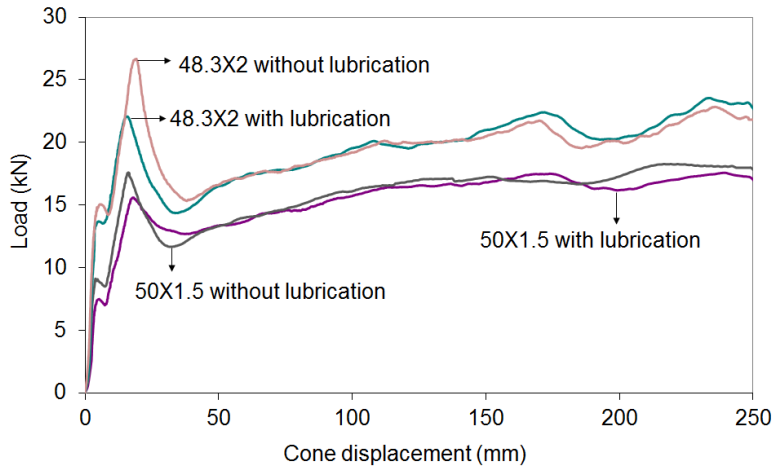


Figure 7: Load – displacement curves of the cone for different D/t

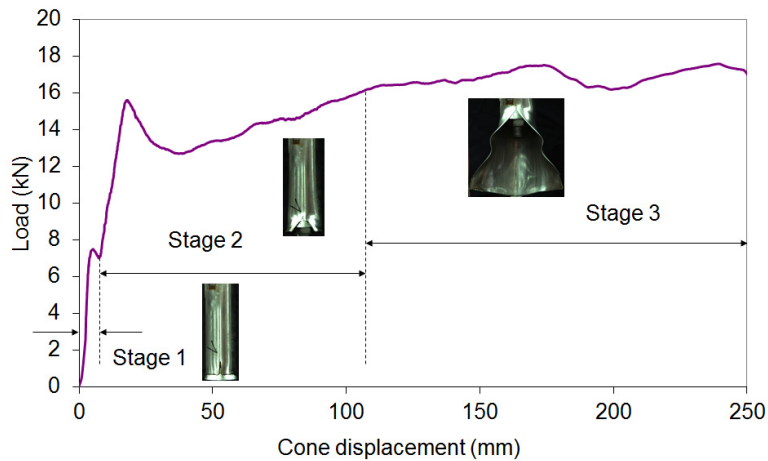


Figure 8: Various zones of behavior curve and associated deformation

### 3 Modeling

#### 3.1 Introduction

For a better analysis (kinematics and stress) in the various zones of the tube, specifically at the crack tip, crack lips and their vicinities, we developed a numerical model using the ABAQUS Standard code. We assume according to experiment observations that only the initial crack propagates along its initial direction. In this potential crack line, the elements that take into account ductile fracture model are introduced. These fracture models used have the capacity to describe the combination of the ductile failure mechanics (nucleation, growth and

coalescence of voids). For the first model (CZM), an interface element was formulated and implemented into ABAQUS Standard via the user subroutine UEL (user element). For the second model (DM), the existing ductile damage formulation in ABAQUS Standard was used. The material behavior was supposed homogeneous and isotropic.

### 3.2 Cohesive model

The interface element has a zero thickness and connects the adjacent elements. When the load increases, the damage can be initiated and be propagated within the interface elements.

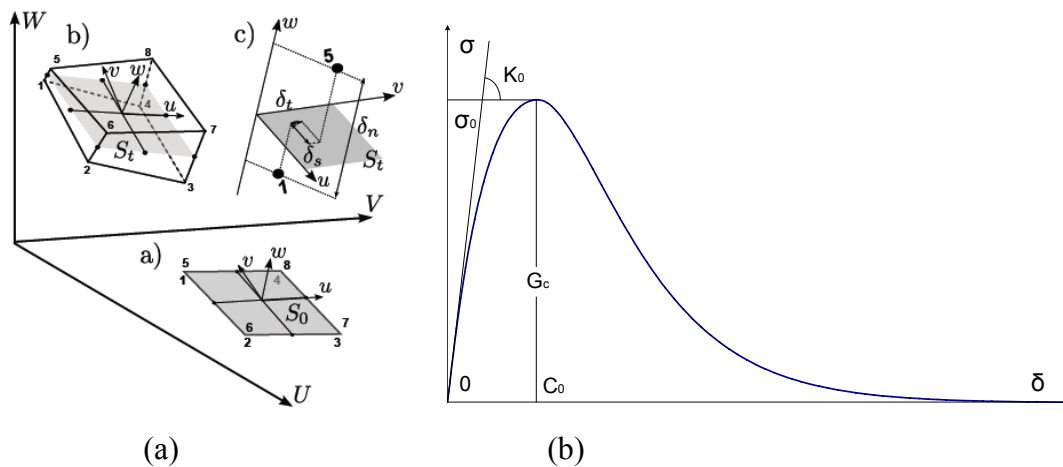


Figure 9: Cohesive model, (a) plane interface element [2], (b) cohesive law [4]

The plane interface element used is composed of 8 nodes with 3 degrees of freedom by node (Figure 9(a)). It is thus compatible with the linear solid element or the linear shell continuum element. In the initial configuration, the 4 higher nodes coincide respectively with the 4 lower nodes. When traction is applied, the nodes separate according to the cohesive law. The element is considered broken when traction is cancelled. The formulation of the 3D cohesive element allows the study in large displacement and rotation [2, 3]. Numerical integration is made according to Newton- Cotes scheme, with 4 integration points. In adequacy with the assumption of a rupture primarily in mode I, the coupling terms in the local stiffness matrix can be set to zero. The diagonal terms of modes II and III are assigned by a dummy value to avoid the numerical singularity. These terms do not influence the result of calculation. For the symmetric half model, the reference plane of the cohesive elements must be located on the symmetric plane. For mode I loading, the modes II and III crack growth are blocked by specific constraints. Among constitutive laws suggested to describe the relation between the stress  $\sigma$  and the separation  $\delta$ , the exponential form (Figure 9(b)) is adopted [4].

$$\sigma = \begin{cases} K_0 \delta e^{-\delta/c_0} & \text{si } \delta \leq c_0 \\ \sigma_0 [1 + \beta(\delta - c_0)] e^{-\beta(\delta - c_0)} & \text{si } \delta > c_0 \end{cases} \quad (1)$$

The constants  $c_0$ ,  $\beta$  are calculated starting from the data of the initial rigidity  $K_0$ , of the maximum stress  $\sigma_0$ , and of the cohesive energy  $G_c$ . The  $K_0$  value must be large enough to ensure the perfect connection between the elements before the initialization of the damage, but sufficiently small to avoid the numerical problem.

### 3.3 Damage model

ABAQUS Standard (version 6.9-2) offers a capacity for modeling progressive damage and failure of ductile metals. In the most general case, this requires the specification on the following:

- the undamaged elastic-plastic response of the material,
- a damage initiation criterion and
- a damage evolution response, including a choice of element removal.

For an elastic-plastic material, damage manifests in two forms: softening of the yield stress and degradation of the elasticity (Figure 10(a)). This damage model supports several types of element. Once a particular initiation criterion is satisfied, the material stiffness is degraded according to the specified damage evolution law for that criterion. Equation (2) shows the damage initiation criterion.

$$\omega_D = \int \frac{d\bar{\varepsilon}^{pl}}{\bar{\varepsilon}_0^{pl}(\eta, \dot{\bar{\varepsilon}}^{pl})} = 1 \quad (2)$$

Where  $\bar{\varepsilon}_0^{pl}$  denotes the equivalent plastic strain where the damage starts,  $\eta$  is the stress triaxiality and  $\dot{\bar{\varepsilon}}^{pl}$  represents the equivalent plastic strain rate.

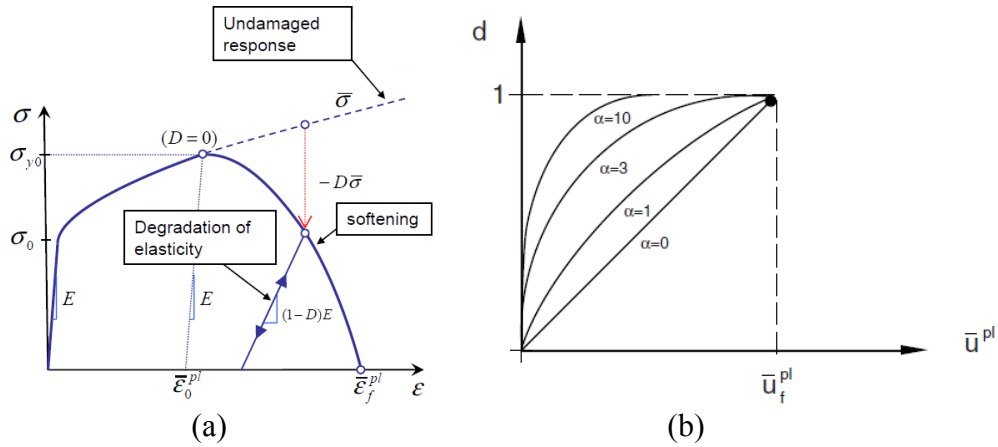


Figure 10: Ductile damage model, (a) damage of elastic-plastic material, (b) exponential form of damage evolution based on plastic displacement [5]

The damage evolution defines the rate of degradation of the material stiffness. The formulation is based on scalar damage approach:

$$\sigma = (1 - D)\bar{\sigma} \quad (3)$$

The overall damage variable  $D$  captures the combined effect of all active damage mechanisms. When damage variable  $D = 1$ , material point has completely failed. The damage evolution law can be specified either in terms of fracture energy or equivalent plastic displacement. Both of these options take into account the characteristic length of the element to alleviate mesh dependency of the results. The evolution of the damage variable with the relative plastic displacement can be specified in tabular, linear, or exponential form. The last form is more used in the calculation for the easy convergence, as shown in Figure 10(b). The damage variable is given as:

$$D = \frac{1 - e^{-\alpha(\bar{u}^{pl} / \bar{u}_f^{pl})}}{1 - e^{-\alpha}} \quad (4)$$

Where,  $\bar{u}_f^{pl}$  is the relative plastic displacement at failure,  $\alpha$  is the exponent.

### 3.4 Numerical simulation

Considering the symmetrical condition, half of tube is modeled by shell continuum elements (SC8R) with three zones of mesh density based on the strain distribution (Figure 11). The cone is modeled with rigid elements R3D4. The contact is defined between slave surface (interior skin of the tube) and master surface (external skin of the cone). The tube is embedded at its base ( $y = 0$ ). Calculations are carried out for the two geometrical configurations (D/t report) and according to two experimental configurations of lubrication. The numerical optimization shows that the use of the friction coefficient equals to 0.15 and 0.2 is reasonable to reproduce respectively the experimental results of the tubes 50x1.5 and 48.3x2.

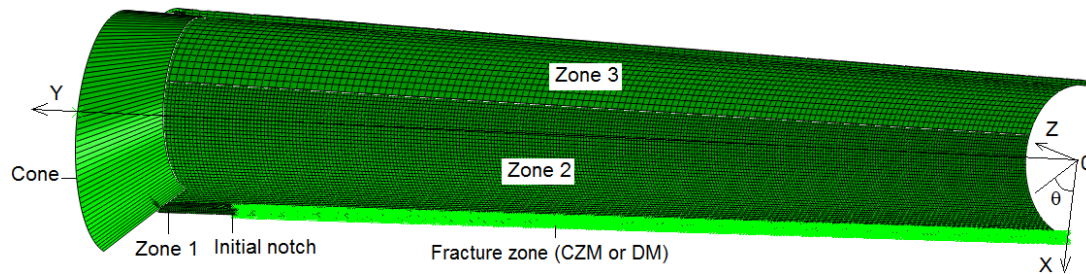


Figure 11: Adopted mesh

In the model with CZM, the cohesive elements size is 0.5mm along the crack propagation direction, with 4 elements through the thickness of the tube. For the half

model, cohesive energy is half of the actual value and rigidity is doubled compared to a complete element. Due to complex problem, the finite element analysis model is often discouraged with non-convergence. The viscous regularization method was implemented to help with numerical difficulties. It consists in conditioning the tangent stiffness matrix for sufficiently small time increments. The use of a small viscosity parameter  $10^{-6}$  helps improve the rate of convergence without compromising results. The material properties for the interface element were chosen as  $K_0 = 1e+5 \times E$  (Mpa/mm) ( $E$  Young's modulus of material),  $\sigma_0 = 1450$ Mpa,  $1/2G_c = 200$ mJ/mm<sup>2</sup>.

In the model with DM, one layer of element SC8R with 0.2mm width in the circumferential direction, taking into account damage model, is considered. These elements have a size of 0.5mm along the crack propagation direction and with 4 elements through the thickness of the tube. The equivalent plastic strain at the initiation of fracture is considered constant in function of stress triaxiality. The equivalent plastic strain rate is equal to zero. The material properties for the DM are chosen as  $\bar{\epsilon}_0^{pl} = 0.3497$ mm/mm (the last strain value of the true stress-plastic strain curve),  $\bar{u}_f^{pl} = 0.13$ mm and  $\alpha = 0.5$ .

Both fracture models predict very well the experimentation. The comparison between the experimental and numerical load-displacement curve corresponding to the tubes 50x1.5 and 48.3x2 is shown in Figure 12 and Figure 14, respectively. The deformed shapes of tube 50x1.5 (Figure 13), 48.3x2 (Figure 15) are similar with that of experimental tests (Figure 5). However, the simulation with CZM is more effective than that with DM in terms of the numerical performance. It consumes less computing time and is easier to converge. For this reason, the other studies later will use CZM. And, the typical tube of 50x1.5 will be considered.

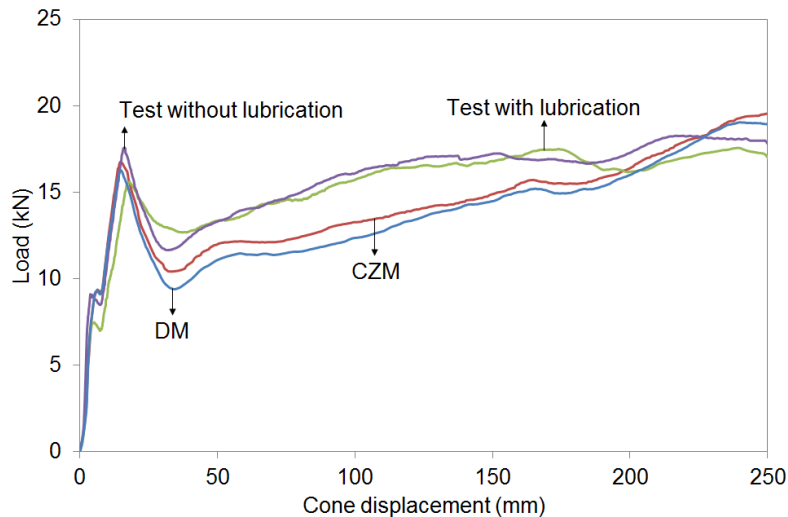


Figure 12: Comparison of experimental and numerical curves for tube 50x1.5

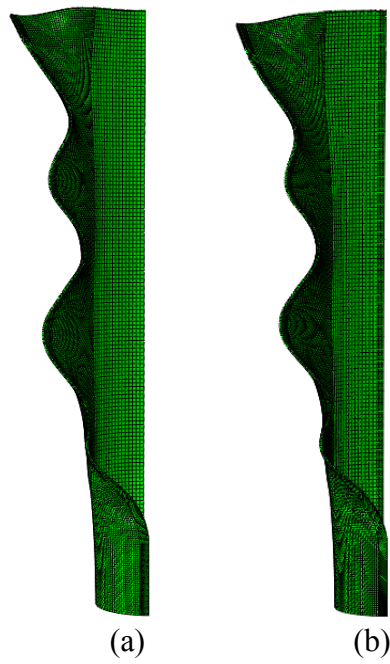


Figure 13: Deformed shapes for tube 50x1.5, (a) CZM, (b) DM

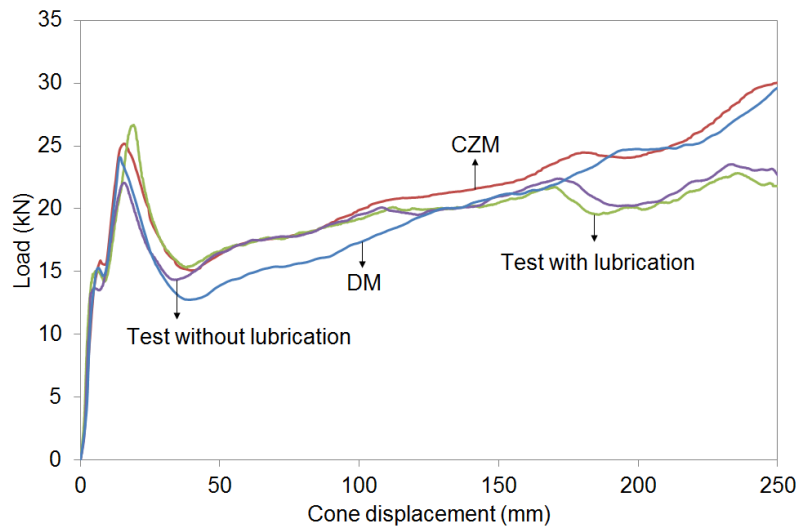


Figure 14: Comparison between experimental and numerical curves for tube 48.3x2

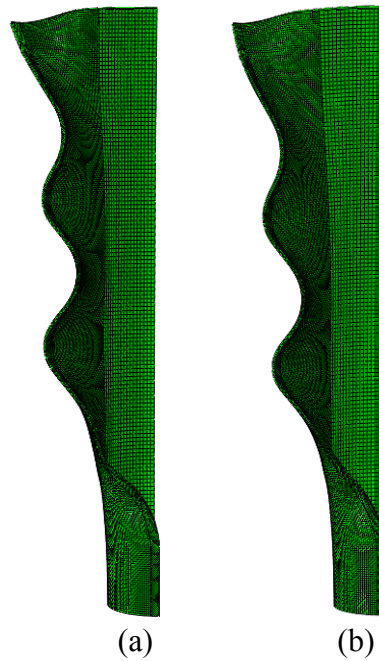


Figure 15: Deformed shapes for tube 48.3x2, (a) CZM, (b) DM

Below, axial membrane strain of the external surface at tube cross-section  $y = 150\text{mm}$  during the tearing is extracted from the case of CZM and is compared to the experimental measurement for the tube 50x1.5 with lubrication (Figure 16). The general trend of the experimental and numerical curves is similar. However, the amplitude of the deformation is different. For numerical calculation, the extraction of the deformation value is carried out at the exact points on the external skin of the tube. However, the deformation measured by the strain gage is regarded as the average deformation at the point in the centre of the gage. The result of measurement becomes less precise when the deformation of the surface occupied by the gage is strongly nonhomogeneous.

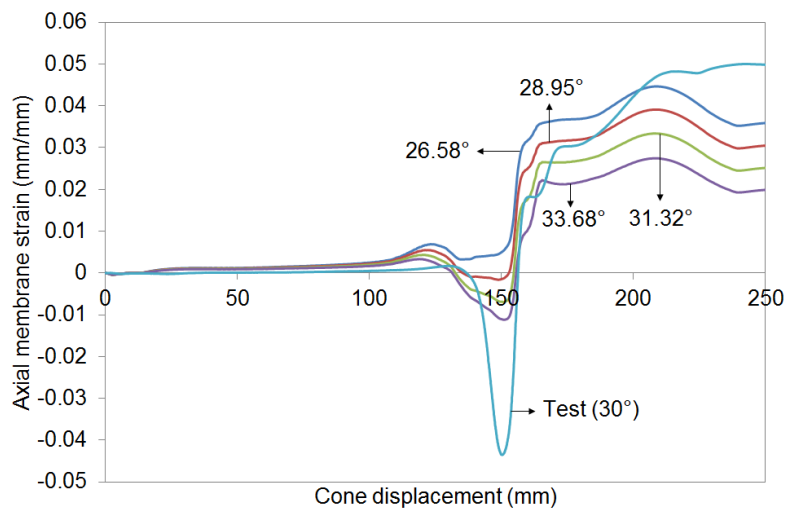


Figure 16: Axial membrane strain in various points at tube cross-section  $y = 150\text{mm}$

To measure performance of element types, we carried out different simulations where the elements size is preserved and the friction coefficient is 0.15. Three cases were considered, one described above, uses the shell continuum element SC8R, the second combines solid elements C3D8I in zone 1, and SC8R in zones 2 and 3, the third model is only made of solid elements C3D8I.

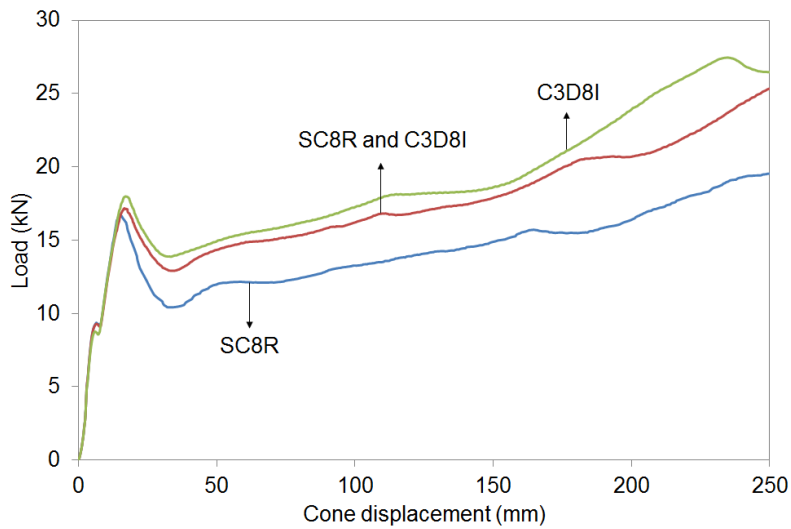


Figure 17: Behavior of tube 50x1.5 according to the element types

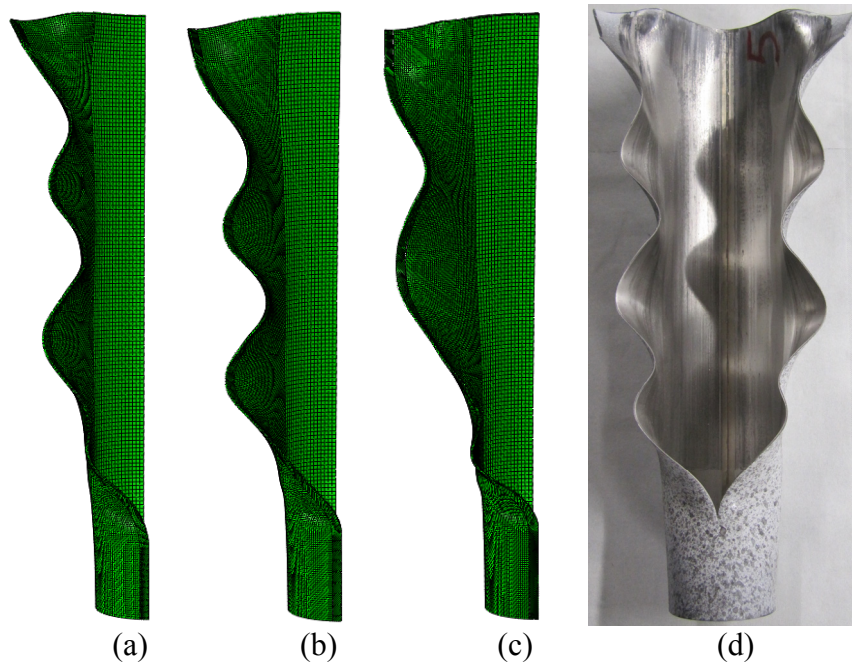


Figure 18: Deformed shapes of tube 50x1.5 according to the element types, (a) SC8R, (b) SC8R and C3D8I, (c) C3D8I, (d) Experiment

The three cases give a quasi-identical behavior regarding the first phase, however the second peak force is different, and these curves are almost parallel (Figure 17). Shell continuum elements seem more flexible than the solid elements, compared to the experimentation, if one considers the deformation, the configuration with SC8R element gives the best results (Figure 18). For solid elements, the increase of mesh density is certainly necessary to capture more accurately the wavelength of the undulations. The computational time for our simulations using a CPU (i5, 4 processors, 2.8GHz) is resumed in Table 1. It shows that the computing time is increase drastically with the number of the solid elements (C3D8I) in the model.

Elements type	SC8R	SC8R & C3D8I	C3D8I
Computing times (h)	10	31	117

Table 1: Numerical performances with the same mesh density

To better understand the role of friction coefficient in numerical results, a variation of this parameter is considered. Three configurations are studied ( $\mu = 0, 0.15, 0.3$ ) and the calculation are carried out using SC8R element. The results show that the friction strongly influences the curve, translating the total behavior (Figure 19). At the same displacement of cone, the load increase with the increase of friction coefficient. But, the general trend of the load-displacement curves is kept. The variation of friction coefficient affects slightly the buckling mode of the tube (Figure 20). The last undulation is more difficult to form with the increase of friction coefficient.

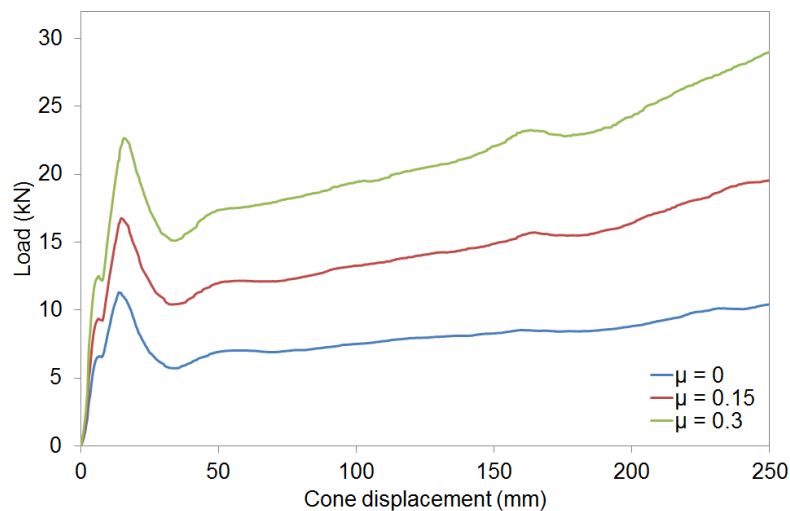


Figure 19: Effect of friction coefficient  $\mu$  on load-deflection curves for tube 50x1.5

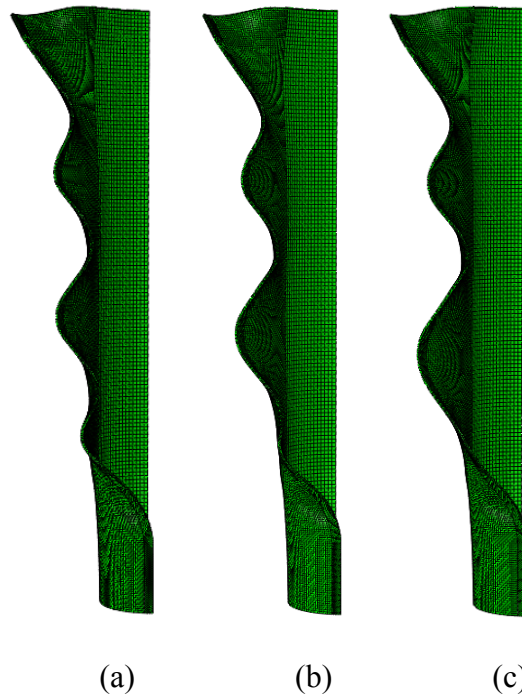


Figure 20: Deformed shapes: tube 50x1.5 (a)  $\mu = 0$ , (b)  $\mu = 0.15$ , (c)  $\mu = 0.3$

### 3.5 Mechanism producing buckling

The tube 50x1.5mm, in the configuration with friction, is here analyzed in details. Analysis of the membrane strain in the medium layer, through the tube thickness, of generalized membrane stress (stress resultant over the tube thickness) at tube cross-section  $y = 150\text{mm}$  gives us the explanation of its deformed shapes. Generator  $\theta = 0^\circ$  corresponds to the crack line. When the cone approaches and passes the studied section, the zones close to the crack lip undergo plastic deformation and the axial deformation dominates the state of membrane deformation (Figure 21, Figure 22, Figure 23, and Figure 24). These plastic deformations are nonhomogeneous at the same time in three directions (axial, circumferential, and radial). We observe a strong variation of thickness in the stretched zones (Figure 25).

The reduced thickness near the fracture zone is caused by the tensile stress at the crack tip which is recognized together in the axial and circumferential directions (Figure 26, Figure 27). A band behind the crack tip is compressed with values of rather large stress (Figure 26). These residual axial compressive efforts generated by the heterogeneity of plastic deformation cause the buckling waves.

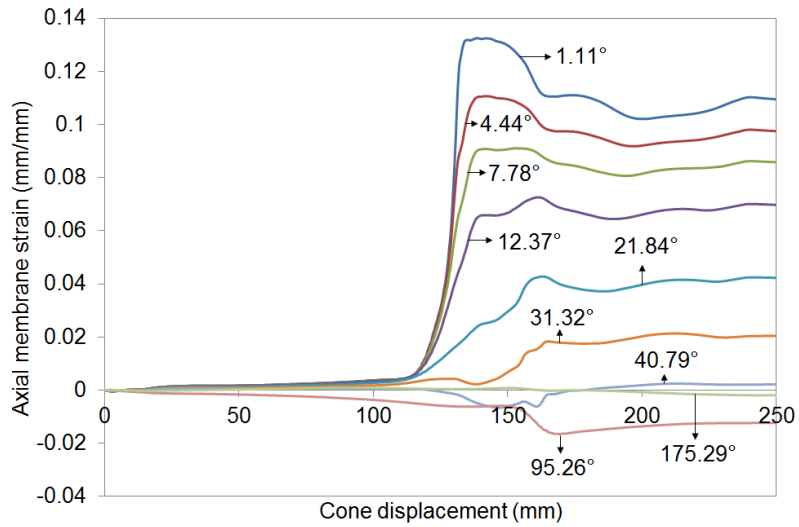


Figure 21: Axial membrane strain at tube cross-section  $y = 150\text{mm}$  during the test

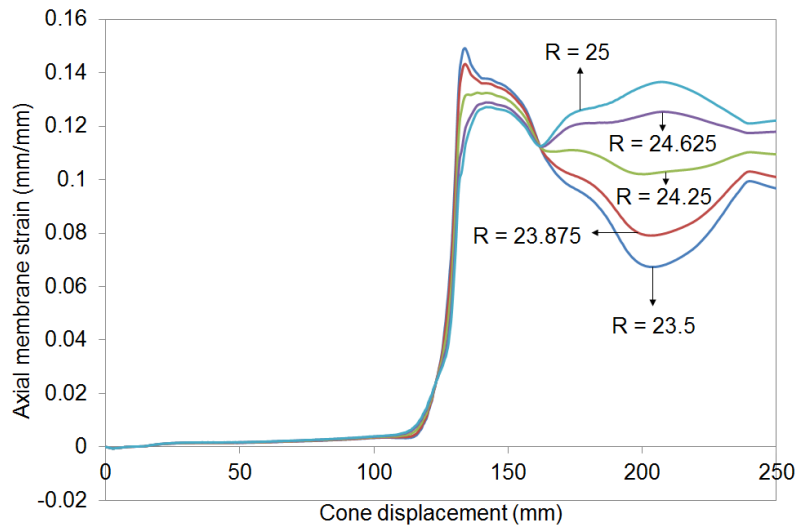


Figure 22: Axial membrane strain through the thickness at tube cross-section  $y = 150\text{mm}$  and  $5^\circ$  from the crack line during the test

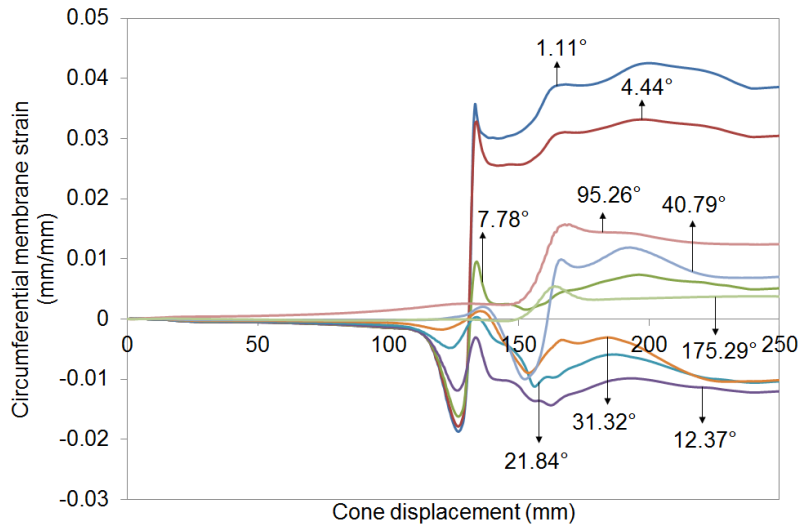


Figure 23: Circumferential membrane strain at tube cross-section  $y = 150\text{mm}$  during the test

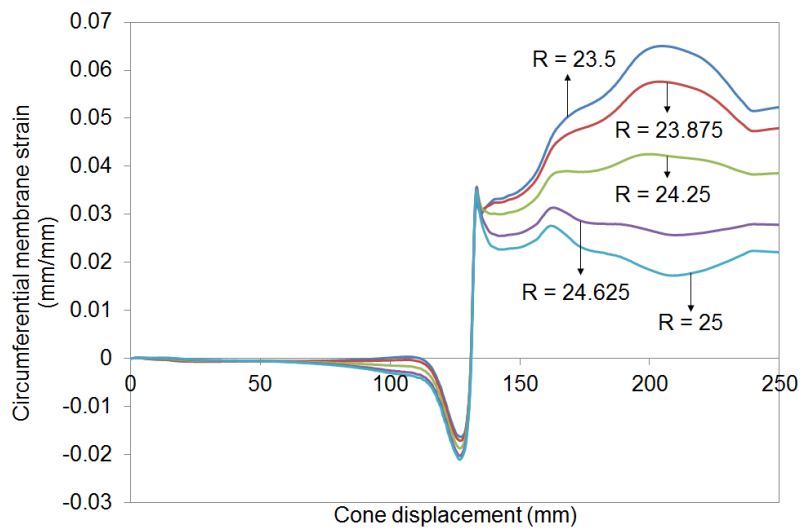


Figure 24: Circumferential membrane strain through the thickness at tube cross-section  $y = 150\text{mm}$  and  $5^\circ$  from the crack line during the test

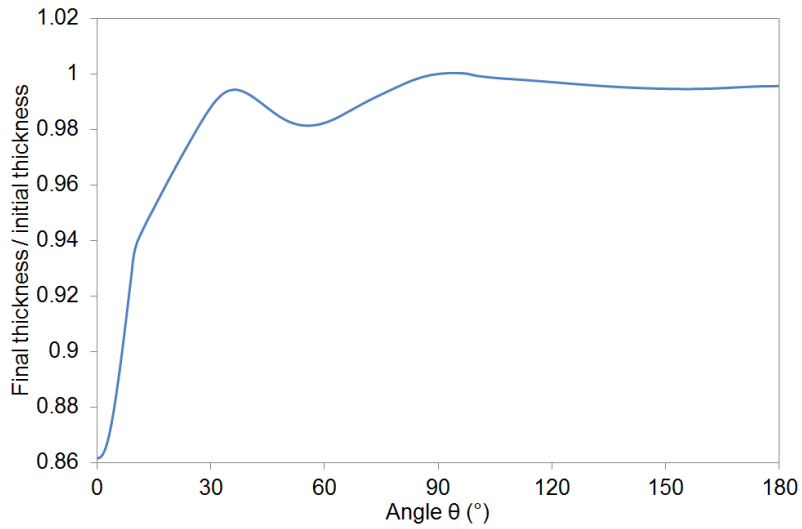


Figure 25: Reduced thickness of the cross-section  $y = 150\text{mm}$  at the end of the test

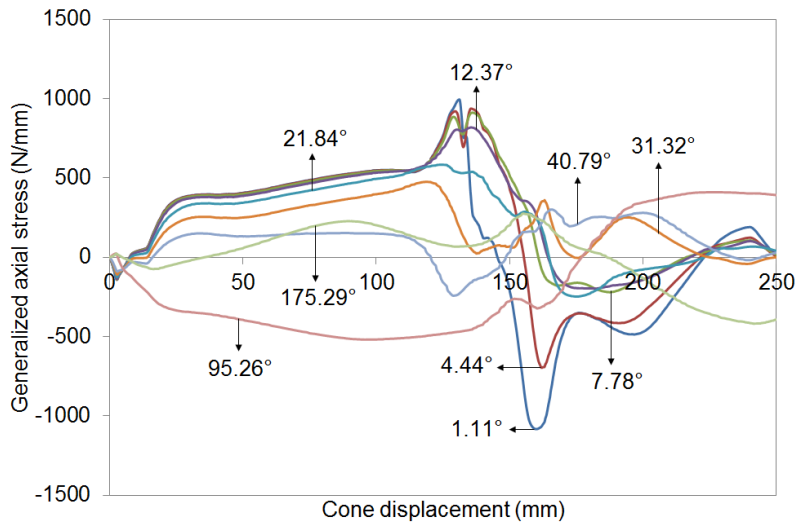


Figure 26: Generalized axial stress at tube cross-section  $y = 150\text{mm}$  during the test

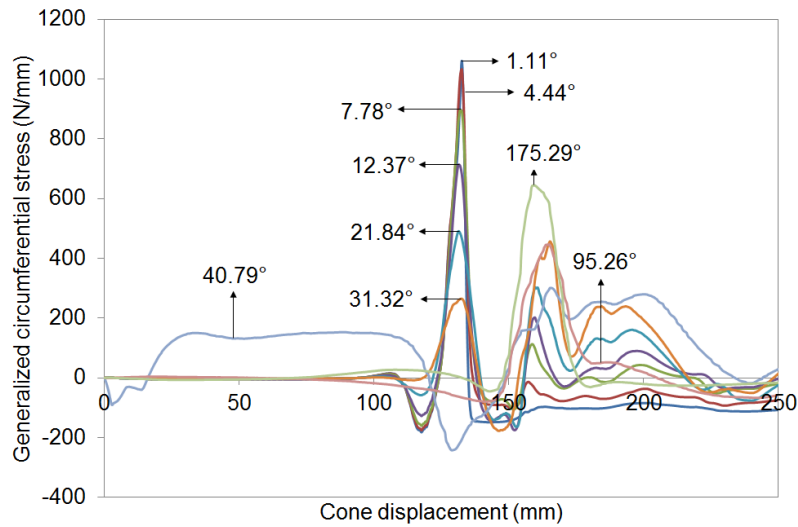


Figure 27: Generalized circumferential stress at tube cross-section  $y = 150\text{mm}$  during the test

## 4 Conclusions

The conducted experimental and numerical studies enabled us to understand the origin of buckling waves which appear on the free edges generated by the operation of “splitting” of tube. To reproduce ductile tearing of metallic tube, two possible modeling are explored, via cohesive zone model CZM or via damage theory DM. Both fracture models can be used to predict the ductile crack propagation. We note however that the CZM is more efficient than DM in terms of numerical performance, and that the quality of the results depends on the nature of the selected elements. The shell continuum elements are less rigid than the linear solid elements and allow capturing the bending inflection, which makes it possible to better corroborate the buckling wavelength.

The axial residual compressive stress acting on a plastic zone causes the appearance of waves on the crack lips. The adopted modeling makes it possible to capture the essential points of physical observations. The next stages aim at considering the influence of the cone dimension, of the various initial defect sizes (crack length), and of the various material types on the tearing behavior.

## References

- [1] Z. Zou, S.R. Reid, “Wavy-edged fractures in axially split aluminum tubes”, *International Journal of Solids and Structures*, 42(16-17), 4519-4540, 2005.

- [2] N. Tardif, A. Combescure, M. Coret and P. Matheron, “Stable crack propagation in steel at 1173K: Experimental investigation and simulation using 3D cohesive elements in large-displacements”, *77(5)*, 776-792, 2010.
- [3] I. Scheider, “Cohesive model for crack propagation analyses of structures with elastic-plastic behavior: Foundations and implantation”, GKSS research center Geesthacht, Dept. WMS, 1-41, 2001.
- [4] G. Alfano, “On the influence of the shape of the interface law on the application of cohesive-zone models”, *Composites Science and Technology*, *66(6)*, 723-730, 2006.
- [5] ABAQUS, “ABAQUS User’s Manual (version 10.2)”, Hibbitt, Karlsson, and Sorensen, Inc, Pawtucket, USA, 2010.